

# A Hexafluorophosphate-Based Ionic Liquid as Multifunctional Interfacial Layer between High Voltage Positive Electrode and Solid-State Electrolyte for Sodium Secondary Batteries

Di Wang, Masaya Takiyama, Jinkwang Hwang,\* Kazuhiko Matsumoto,\* and Rika Hagiwara

Sodium secondary batteries have gained accolades as future energy storage devices due to their low costs and environmental benignity, but are heavily impeded by the poor anodic stabilities of most electrolytes, including solid-state electrolytes (SSE), that render them incompatible with high-voltage positive materials. This study reports, for the first time, a new synthesis technique using a fluorohydrogenate ionic liquid (IL) precursor to prepare a [DEME][PF<sub>6</sub>] ([DEME]<sup>+</sup>: *N,N*-diethyl-*N*-methyl-*N*-(2-methoxyethyl) ammonium) with high yield and high purity. Herein, a Na[PF<sub>6</sub>]-[DEME][PF<sub>6</sub>] IL is formulated and subjected to a series of electrochemical tests to validate its performance in battery applications. The present IL harbors a strong oxidative stability (up to 5.2 V on Pt and >4.5 V on conductive carbon electrodes) that aids in the suppression of oxidative decompositions of one typical SSE, for example, beta alumina solid electrolyte (BASE), thereby extending their electrochemical window in hybrid SSE systems. A hybrid solid-state Na secondary battery employing a high voltage positive electrode, Na<sub>3</sub>V<sub>2</sub>(PO<sub>4</sub>)<sub>2</sub>F<sub>3</sub>, is assembled using the BASE/IL configuration, and features energy density and superior cycling performance. This work demonstrates that sandwiching an SSE between the oxidatively stable [PF<sub>6</sub>]<sup>−</sup> IL can be an effective design for high voltage operation Na secondary batteries.

campaigns toward a sustainable society. In line with this ecological motif, the low cost and abundance of Na resources have sparked considerable interest in Na secondary battery technologies for large-scale utilities such as grid energy storage. However, the low energy densities of Na secondary batteries (compared to their Li counterparts) present a key challenge to their viability, necessitating the exploration of high-voltage positive electrode materials to increase their operating voltages.<sup>[1]</sup> Among the prominent high-voltage positive electrode materials, layered oxides such as NaNi<sub>x</sub>Mn<sub>1−x</sub>O<sub>2</sub>, Na<sub>2/3</sub>MnO<sub>2</sub>,<sup>[2]</sup> and polyanionic compounds such as Na<sub>3</sub>V<sub>2</sub>(PO<sub>4</sub>)<sub>2</sub>O<sub>2−2x</sub>F<sub>1+2x</sub>,<sup>[3]</sup> have been reported to exemplify high operating potentials of up to 4.5 V versus Na<sup>+</sup>/Na. Even so, the practicality of high-voltage positive electrodes is heavily hampered by their poor compatibility with conventional organic electrolytes, which typically entail carbonates that decompose

before reaching the high upper cut-off voltages, resulting in limited capacities and low Coulombic efficiencies.<sup>[1,4]</sup> To optimize the stability of organic electrolytes, additives such as fluoroethylene carbonate,<sup>[5]</sup> dimethyl carbonate,<sup>[6]</sup> and lithium difluorobis(oxalato) phosphate<sup>[7]</sup> have been explored for their ability to form robust cathode electrolyte interface (CEI) layers that mitigate electrolyte oxidation during high-voltage operations. Elevated temperatures have also been reported to cause continuous decomposition of organic electrolytes, resulting in significant capacity degradation and low Coulombic efficiencies even in the presence of additives.<sup>[8]</sup> In addition, organic electrolytes have raised safety concerns attributed to their high volatility and flammability. Consequently, solid-state electrolytes (SSEs) have gained traction as providential electrolyte candidates for Na metal batteries due to their high thermal stabilities and specific energies (e.g., when utilizing Na metal negative electrodes and compact stacking).<sup>[9]</sup>

Beta alumina solid electrolyte (BASE) is a renowned SSE and a well-established Na ion conductor with ionic conductivities

## 1. Introduction

Electrochemical energy storage systems, particularly secondary batteries, have become quintessential facets in the ongoing

D. Wang, M. Takiyama, J. Hwang, K. Matsumoto, R. Hagiwara  
Fundamental Energy Science Department  
Graduate School of Energy Science  
Kyoto University  
Yoshida-honmachi, Sakyo-ku, 606-8501 Kyoto, Japan  
E-mail: hwang.jinkwang.5c@kyoto-u.ac.jp;  
matsumoto.kazuhiko.4c@kyoto-u.ac.jp

The ORCID identification number(s) for the author(s) of this article can be found under <https://doi.org/10.1002/aenm.202301020>

© 2023 The Authors. Advanced Energy Materials published by Wiley-VCH GmbH. This is an open access article under the terms of the Creative Commons Attribution License, which permits use, distribution and reproduction in any medium, provided the original work is properly cited.

DOI: 10.1002/aenm.202301020

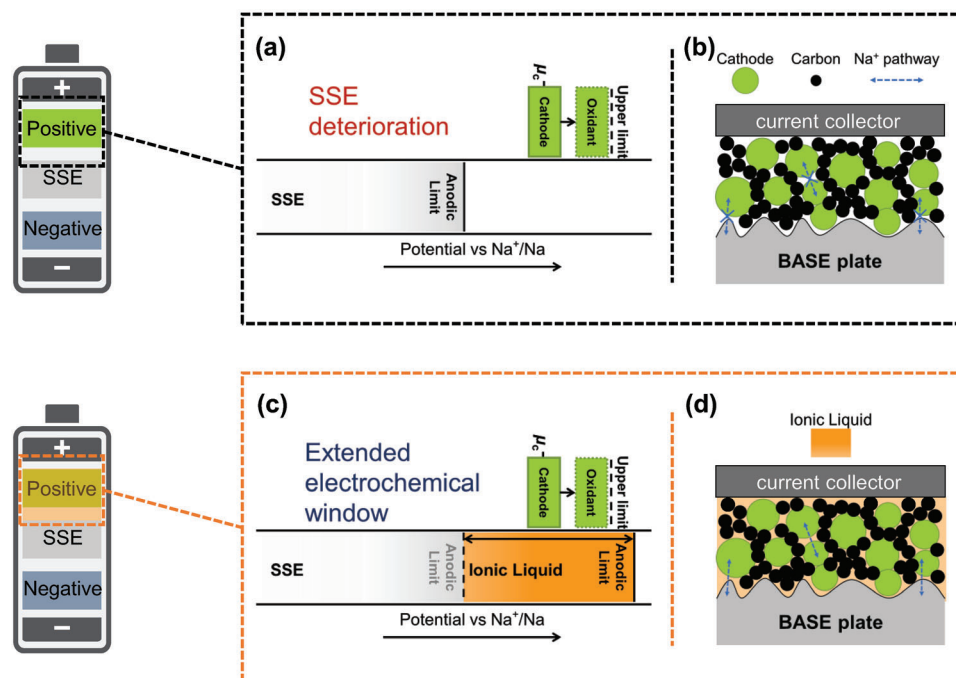


**Figure 1.** Schematic diagram about the interfacial issues and anodic limit of a solid-state electrolyte (SSE), and a strategy of ionic liquid as an interfacial layer between a positive electrode and a SSE for Na secondary battery; a) an example of the anodic limit of a SSE and the potential profile of a high voltage positive electrode—the chemical potential of the positive electrode ( $\mu_c$ ) is beyond the anodic limit of the SSE. b) Insufficient Na ion pathway within solid–solid SSE/positive electrode (poor contact). c) The extended electrochemical window of hybrid SSE and d) improved Na ion pathway within hybrid SSE/electrode (facile contact) achieved by incorporating an IL.

that magnitudes in the order of  $10^{-3} \text{ S cm}^{-1}$  at room temperatures, depending on the crystal state, treatment temperature, and dopants.<sup>[9a]</sup> This SSE is known to have a low cathodic limit (reduction potential) that enables the use of Na metal negative electrodes over wide temperature ranges.<sup>[9a,10]</sup> Although practical cell tests using BASE have shown the upper potential can go up to 4.5 V versus  $\text{Na}^+/\text{Na}$ ,<sup>[11]</sup> some experimental works along with density functional theory (DFT) calculations have shown BASE to have a lower limit of oxidative stability: ranging from 3.0 to 3.8 V versus  $\text{Na}^+/\text{Na}$ .<sup>[12]</sup> As illustrated in **Figure 1a**, higher chemical potentials of a positive electrode ( $\mu_c$ ) beyond the anodic limit of the SSE might be able to cause SSE deterioration at the interface upon the positive electrode, resulting in increased interfacial resistance and overall overvoltage.<sup>[9b]</sup> Moreover, all-solid-state batteries employing SSEs generally exhibit limited electrochemical performance caused by high resistances at the electrolyte/electrode interface due to the poor solid–solid contact (so-called mechanical contact, see **Figure 1b**), providing insufficient Na ion pathway within the solid–solid SSE/positive electrode.<sup>[9a,12c,13]</sup> In a word, facilitating the contact between the SSE and positive electrodes is pivotal for the chemical, electrochemical, and durable issues.<sup>[14]</sup> From these limitations, the implementation of hybrid SSEs wherein a rigid SSE is used as the main ionic conductor alongside secondary ionic conductors made from soft materials such as organic electrolytes,<sup>[15]</sup> polymers<sup>[16]</sup> or ionic liquids (ILs),<sup>[17]</sup> can be considered a prudent strategy for ensuring sufficient contact between the electrode and the SSE and extend electrode chemical window of the SSE

(**Figure 1c,d**). However, the use of organic electrolytes spoils one of the great advantages of SSEs, “high safety.”

In the context of secondary ion conductors for hybrid SSEs, ILs represent a prime class of electrolytes with remarkable compositional diversity that allows operations with an assortment of electrode materials. These “liquid-state salts” exclusively consist of cations and anions—a characteristic that renders their physicochemical and electrochemical properties highly tunable through the selection of appropriate ion combinations.<sup>[18]</sup> Among the anionic species for ILs,  $[\text{PF}_6]^-$  has been established to have relatively profound oxidative stability through linear sweep voltammetry (LSV)<sup>[19]</sup> and DFT calculations of its highest occupied molecular orbital (HOMO) energy, which has been associated with oxidation potentials in some cases.<sup>[20]</sup> It should be mentioned that the HOMO energy alone cannot sufficiently establish the practical anodic limits for electrochemical windows.<sup>[21]</sup> However, based on the anodic stability trends projected by HOMO energy calculations,  $[\text{PF}_6]^-$ -based ILs show higher oxidative stabilities than the  $[\text{BF}_4]^-$ ,  $[\text{TFSA}]^-$  (bis(trifluoromethanesulfonyl)amide)-, and  $[\text{FSA}]^-$  (bis(fluorosulfonyl)amide)-based ILs. To adequately ascertain the anodic limits of ILs, it is also important to take into consideration the influence of the cation selected. For instance,  $[\text{C}_4\text{C}_1\text{im}]^+$  (1-butyl-3-methylimidazolium), one of the most common counter-cation for room temperature  $[\text{PF}_6]^-$  based ILs, has been predicted to oxidize at a lower potential than  $[\text{PF}_6]^-$  according to calculations.<sup>[20b]</sup> On the other hand, non-aromatic ammonium ions, like  $[\text{C}_3\text{C}_1\text{pyrr}]^+$  (*N*-methyl-*N*-propylpyrrolidinium), are supposed to possess higher anodic stability when combined

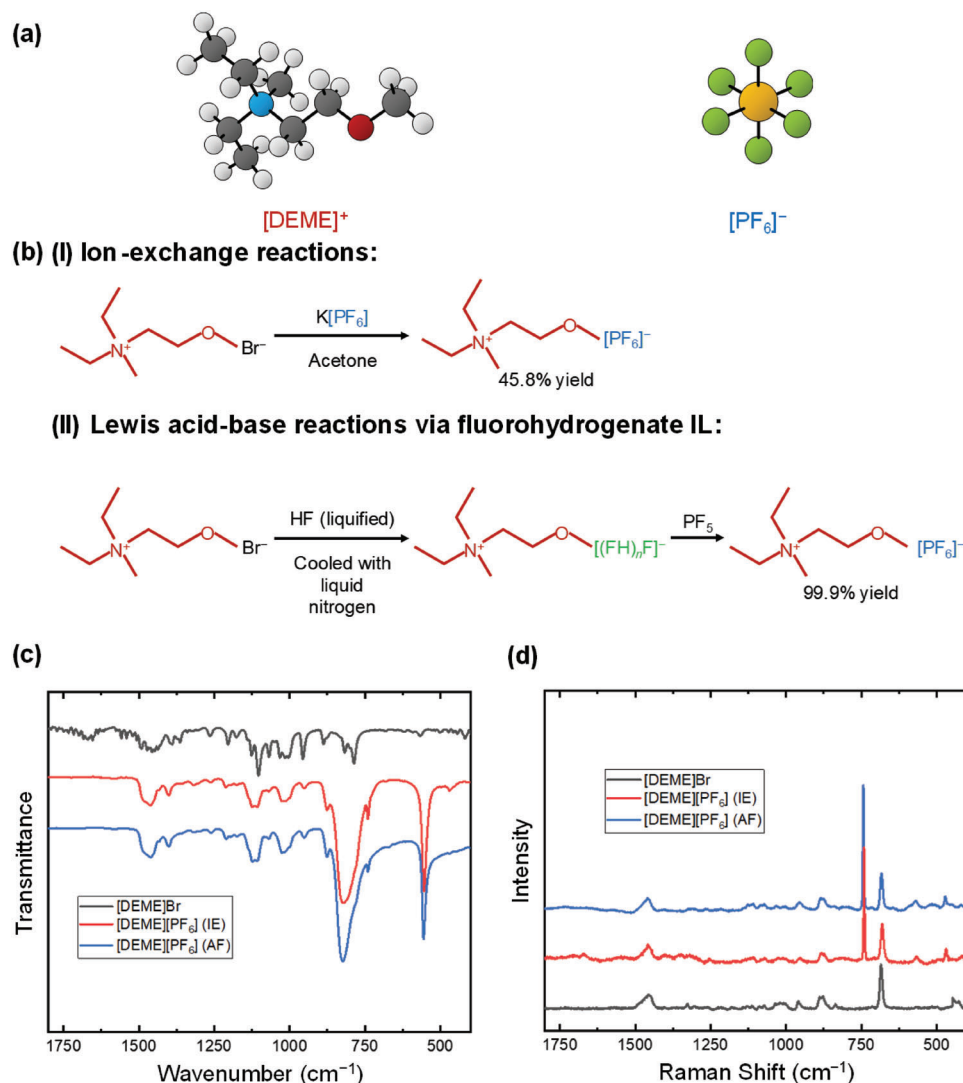


**Figure 2.** a) Molecular structures of [DEME]<sup>+</sup>: *N,N*-diethyl-*N*-methyl-*N*-(2-methoxyethyl)ammonium cation, [PF<sub>6</sub>]<sup>-</sup>: hexafluorophosphate anion. b) Schematic of two synthesis routes of [DEME][PF<sub>6</sub>] based on (I) ion-exchange reaction (IE) and (II) Lewis acid–base reaction via fluorohydrogenate IL (AF) reaction. c) Infrared spectra and d) Raman spectra of [DEME]Br and [DEME][PF<sub>6</sub>] prepared by IE and AF reaction, respectively, in the region between 400 and 1800 cm<sup>-1</sup>.

with [PF<sub>6</sub>]<sup>-</sup>.<sup>[20b]</sup> Even so, the practicality of this salt as an electrolyte for batteries is significantly impeded by its high melting point (>113 °C).<sup>[22]</sup> In fact, only a limited number of cations are capable of providing melting points below ambient temperatures when combined with [PF<sub>6</sub>]<sup>-</sup> due to the high symmetry, rigidity, and relatively small radius of [PF<sub>6</sub>]<sup>-</sup>. Additionally, [PF<sub>6</sub>]<sup>-</sup>-based IL electrolytes are plagued with high viscosities,<sup>[23]</sup> which present considerable constraints in their utility as battery electrolytes.

Among the cations available for combination with the [PF<sub>6</sub>]<sup>-</sup> to form salts, the [DEME]<sup>+</sup> (*N,N*-diethyl-*N*-methyl-*N*-(2-methoxyethyl) ammonium, **Figure 2a**) cation is considered a promising candidate due to the asymmetric structure with the flexible methoxyethyl group,<sup>[24]</sup> which assists the reduction of melting point. The practicality of this cation is further bolstered by the non-aromaticity of [DEME]<sup>+</sup>, which proffers a higher anodic limit.<sup>[25]</sup> It is worth noting that although [DEME][PF<sub>6</sub>] IL is

known to be liquid at 25 °C, its utility in batteries has yet to be realized due to its undesirable viscosity.<sup>[26]</sup>

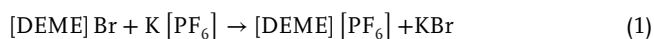
In a bid to augment the practical viability of Na secondary batteries aimed at high-voltage operations, this work reports, for the first time, a highly efficient synthesis route for [DEME][PF<sub>6</sub>] IL. A Na[PF<sub>6</sub>]-[DEME][PF<sub>6</sub>] IL system was formulated and subjected to physicochemical measurements to establish its suitability for a hybrid SSE made from the IL and BASE. The present IL is found to play the multifunctional role of suppressing the oxidative decomposition of the BASE while improving the surface contact between a positive electrode and BASE (Figure 1c,d). To harness the electrochemical capabilities of the Na<sub>3</sub>V<sub>2</sub>(PO<sub>4</sub>)<sub>2</sub>F<sub>3</sub> (NVPF) positive electrode, a hybrid solid-state cell was implemented, utilizing the BASE/Na[PF<sub>6</sub>]-[DEME][PF<sub>6</sub>]/NVPF as the positive cell component. The NVPF positive electrode in this configuration exhibits typical behavior characterized by two redox plateaus at

high potentials of 3.7 and 4.2 V versus Na<sup>+</sup>/Na—attesting to the compatibility high compatibility between the present battery components.<sup>[27]</sup>

## 2. Results and Discussion

### 2.1. Synthesis and Characterization of [DEME][PF<sub>6</sub>]

The compositional diversity of ILs proffers a number of preparation methods depending on the physical and chemical properties of the materials involved. Among the synthesis methodologies, the ion exchange (IE) reaction (also known as metathesis) between an organic halide salt and an alkali metal salt is considered one of the most straightforward routes for preparing ILs.<sup>[28]</sup> As illustrated in Figure 2b[I], the present study employed the IE reaction (Equation (1)) between [DEME]Br and K[PF<sub>6</sub>] with the aid of an anhydrous acetone solvent to prepare [DEME][PF<sub>6</sub>].



Upon completion of the reaction, the sedimentary KBr was filtered, and the solvent was removed. Subsequently, the resultant [DEME][PF<sub>6</sub>] was repeatedly washed using water to remove the residual KBr. It should be mentioned here that [DEME][PF<sub>6</sub>] is not hydrophobic enough to facilitate an effective separation from an aqueous phase. Therefore, a certain amount of [DEME][PF<sub>6</sub>] dissolved into the aqueous phase during each round of extraction, resulting in a low yield of 45.8%.

Given the low yield from the conventional IE route, the adoption of a more efficient preparation method can be posited to improve the practical utility of [DEME][PF<sub>6</sub>]. According to previous reports, a Lewis acid–base reaction entailing a fluorohydrogenate IL (AF) has been an effective approach for synthesizing several ILs with fluorocomplex anions.<sup>[29]</sup> In a bid to capitalize on this technique, the AF reaction was also implemented to synthesize [DEME][PF<sub>6</sub>]. As shown in Figure 2b[II], an initial reaction (Equation (2)) between [DEME]Br and anhydrous HF was performed to form the [DEME][(FH)<sub>n</sub>F] fluorohydrogenate IL. Given that the F<sup>−</sup> in the [(FH)<sub>n</sub>F]<sup>−</sup> anion is coordinated by multiple HF (*n* is the number of HF in [(FH)<sub>n</sub>F]<sup>−</sup>) through characteristically strong hydrogen bonds,<sup>[30]</sup> the intermediate HBr byproduct could easily be removed through gaseous evacuation. In the subsequent AF reaction (Equation (3)), [PF<sub>6</sub>]<sup>−</sup> was generated via Lewis acid–base reaction between F<sup>−</sup> and PF<sub>5</sub>, and simultaneously HF was liberated to yield 99.9% [DEME][PF<sub>6</sub>] with a high level of purity.



The synthesis flow chart and the reaction line for the reaction are provided in Figures S1 and S2, Supporting Information. The elemental composition of the reaction products from both preparation methods was validated through elemental analysis, where the C, H, N, and F analytical values were confirmed to be consistent with the theoretical values (see Experimental Section). The Br content was also determined to be below the detection limits of the AgNO<sub>3</sub> test for both reaction products. The

purity of the [DEME][PF<sub>6</sub>] products was also quantitatively established through nuclear magnetic resonance (NMR) spectroscopy (<sup>1</sup>H and <sup>19</sup>F), wherein both reaction products were found to have purity levels above 99% (see Experimental Section).

For further characterization, the Fourier transform infrared spectra (FT-IR) of the [DEME][PF<sub>6</sub>] synthesized via the IE and AF routes were obtained alongside those of [DEME]Br, as shown in Figure 2c. The IR spectra of [DEME][PF<sub>6</sub>] from both cases exhibited absorption bands for the ν<sub>3</sub> and ν<sub>4</sub> modes of [PF<sub>6</sub>]<sup>−</sup> at 882 and 560 cm<sup>−1</sup>, respectively.<sup>[31]</sup> The other absorption bands appeared comparable to those in the [DEME]Br spectrum and were thus assigned to [DEME]<sup>+</sup>. The IR spectra indicate that the [DEME][PF<sub>6</sub>] prepared through the AF route is virtually identical to the one prepared via the IE route. Raman spectra of the [DEME][PF<sub>6</sub>] from both preparation routes were also obtained alongside the [DEME]Br spectrum, as shown in Figure 2d. The spectra depict characteristic peaks at 743, 569, and 471 cm<sup>−1</sup> that were assigned to the ν<sub>1</sub>, ν<sub>2</sub>, and ν<sub>5</sub> modes of [PF<sub>6</sub>]<sup>−</sup>, respectively.<sup>[32]</sup> Comparing the two [DEME][PF<sub>6</sub>] spectra with the [DEME]Br spectrum further validates that the other peaks could be assigned to the vibrational modes of the [DEME]<sup>+</sup> cation.<sup>[33]</sup>

### 2.2. Physicochemical and Electrochemical Characterization

For investigations into the physicochemical and electrochemical properties of the [DEME][PF<sub>6</sub>], a Na[PF<sub>6</sub>]-[DEME][PF<sub>6</sub>] IL system was formulated by dissolving Na[PF<sub>6</sub>] salt into the [DEME][PF<sub>6</sub>] at the molar ratio of 10:90 mol%. This molar ratio embodies the maximum possible concentration of the Na[PF<sub>6</sub>] salt (10 mol%) in [DEME][PF<sub>6</sub>]. The density of the Na[PF<sub>6</sub>]-[DEME][PF<sub>6</sub>] IL system was measured at temperatures varied from 10 to 90 °C and the results were then used to calculate the molar concentrations of Na[PF<sub>6</sub>] (see Tables S1 and S2, Supporting Information, for the density and molar concentration data). The correlation between the temperature and the density of the present IL system is illustrated in Figure 3a. Here, the density and molar concentration of the current system is seen to decrease linearly with increasing temperature. The IL system was noted to have a molar concentration of Na[PF<sub>6</sub>] of 0.501 mol dm<sup>−3</sup> at 25 °C. The correlation between the temperature and the viscosity (η) and ionic conductivity (σ) of the Na[PF<sub>6</sub>]-[DEME][PF<sub>6</sub>] IL systems were also assessed at temperatures varied from 10 to 90 °C, as shown in Figures 3b and 3c, respectively (see Tables S3 and S4, Supporting Information, for the viscosities and ionic conductivities data). As with common ILs, increasing the temperature of the present system was noted to decrease the viscosity and increase the ionic conductivity of the present system. At 30 °C, the viscosity of the Na[PF<sub>6</sub>]-[DEME][PF<sub>6</sub>] IL (1930 mPa s) was observed to be relatively higher than those of common IL systems (e.g., 28.9 mPa s for 10 mol % Na[FSA]-[C<sub>2</sub>C<sub>1</sub>im][FSA]).<sup>[34]</sup> Correspondingly, the ionic conductivity at 30 °C is 0.25 mS cm<sup>−1</sup>: a relatively lower value than those of common ILs electrolytes for energy storage devices (e.g., 12.2 mS cm<sup>−1</sup> for 10 mol% Na[FSA]-[C<sub>2</sub>C<sub>1</sub>im][FSA]).<sup>[34]</sup> As shown in Figure S3, Supporting Information, a Na<sup>+</sup> transference number of 0.15 was derived from bulk and diffusion resistances obtained through very low frequency-impedance spectroscopy performed on a symmetric Na/IL/Na cell at 25 °C.<sup>[35]</sup> The physicochemical properties of the present Na[PF<sub>6</sub>]-[DEME][PF<sub>6</sub>]



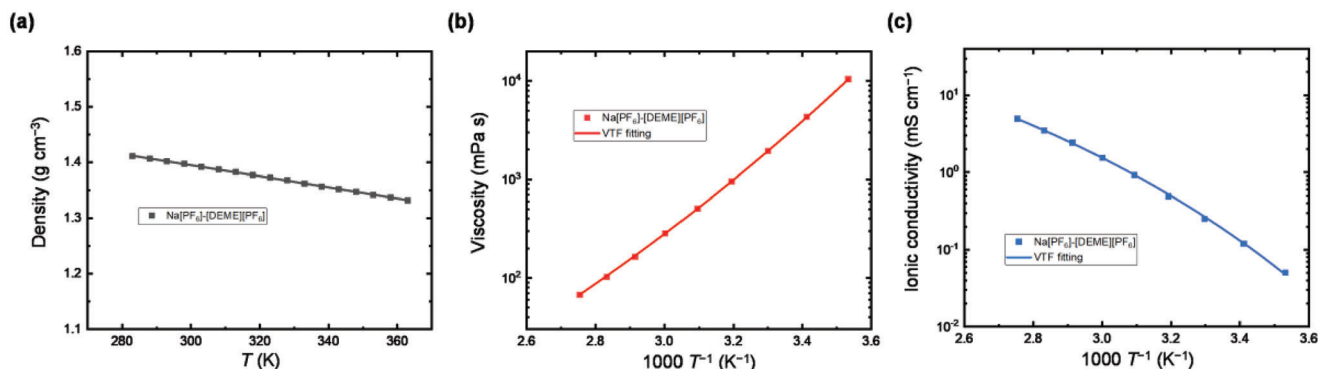


**Figure 3.** Physicochemical properties of [DEME][PF<sub>6</sub>] with 10 mol% Na[PF<sub>6</sub>]: Temperature dependence of a) density, b) viscosity, and c) ionic conductivity. Density was fitted with a linear relation against temperature. Viscosity and ionic conductivity were fitted with the VTF relation.

IL system are consistent with those from a previous report where this IL was found to exhibit a relatively high melting point and viscosity.<sup>[26]</sup> Notably, the Arrhenius plots for viscosity and ionic conductivity form concave and convex shapes, respectively, indicating that they can be well-fitted with the Vogel–Tammann–Fulcher (VTF) equations below (Equations (4) and (5)).<sup>[36]</sup>

$$\eta(T) = A_{\eta} \sqrt{T} \exp\left(-\frac{B_{\eta}}{T - T_{0\eta}}\right) \quad (4)$$

$$\sigma(T) = \frac{A_{\sigma}}{\sqrt{T}} \exp\left(-\frac{B_{\sigma}}{T - T_{0\sigma}}\right) \quad (5)$$

The resulting VTF fitting parameters are shown in Tables S5 and S6, Supporting Information. Here, the  $A_{\sigma}$ ,  $B_{\sigma}$ ,  $A_{\eta}$ , and  $B_{\eta}$  represent the fitting parameters, whereas the  $T_{0\eta}$  and  $T_{0\sigma}$  denote constants for the ideal glass transition temperatures for viscosity and ionic conductivity, respectively. In general, a Walden plot is employed to interpret the correlation between the molar conductivity ( $\Lambda$ ) and viscosity of an electrolyte.<sup>[37]</sup> For IL systems, the fractional Walden rule (Equation (6)) is often used for a non-unity gradient in the Walden plot instead of the Walden rule (whereby,  $\alpha = 1$  in the following relation):

$$\Lambda \eta^{\alpha} = \text{constant} \quad (6)$$

The  $\alpha$  here is a constant between zero and unity correlated with the degree of dissociation.<sup>[36c,38]</sup> A dashed line provided in Figure S4, Supporting Information, is used as a visual guide to clearly visualize the point where  $\alpha$  equals 1. According to a previous report, the relative position between the IL electrolytes and this dashed line is an indicator of the ion transport properties of the electrolytes.<sup>[38]</sup> The slope  $\alpha$ , which corresponds to the ratio of activation energies of viscosity and ionic conductivity, was determined to be 0.948 for the present Na[PF<sub>6</sub>]-[DEME][PF<sub>6</sub>] IL. This value is comparable to those of common ILs, indicating that the present system hosts archetypal ion conduction mechanisms.<sup>[39]</sup>

The cathodic and anodic limits, which typically define the electrochemical window of an electrolyte, are considered crucial parameters that define its compatibility with the electrode materials. As such, LSV measurements were performed on the Na[PF<sub>6</sub>]-[DEME][PF<sub>6</sub>] IL electrolyte in comparison with a com-

mon IL electrolyte: Na[FSA]-[C<sub>2</sub>C<sub>1</sub>im][FSA] ([C<sub>2</sub>C<sub>1</sub>im]<sup>+</sup>: 1-ethyl-3-methylimidazolium, which is also used in the electrochemical test below) to assess their electrochemical stability. As shown in Figure 4a, the anodic limit of the Na[FSA]-[C<sub>2</sub>C<sub>1</sub>im][FSA], is demonstrated by a sharp rise in current at 4.5 V at the Pt working electrode at a scan rate of 1 mV s<sup>-1</sup> (threshold current density: 0.01 mA cm<sup>-2</sup>). On the other hand, the Na[PF<sub>6</sub>]-[DEME][PF<sub>6</sub>] IL exhibited only a weak current response around 5.2 V (threshold current density: 0.01 mA cm<sup>-2</sup>): an indication of the high oxidation stability of the electrolyte.

To augment the practicality of Na secondary battery systems operating at high voltage, it is essential to explore their possible utility alongside common SSEs. It is important to note that the limited contact area between SSEs and current collectors and the slow decomposition reaction kinetics make it challenging to estimate their oxidation limits accurately.<sup>[40]</sup> As a solution, some studies have proposed SSE-C composite working electrodes using powdered SSE acting as an “active material” in conventional cells mixed with conductive carbon to obtain sufficient electronic contact.<sup>[41]</sup> In a bid to exploit this avenue, the present study investigated a working electrode (BASE-C electrode) comprising BASE powder and acetylene black (AB) in comparison to an AB carbon working electrode (C electrode) to assess the oxidation limitations of BASE and IL electrolytes. The schematics of the electrode configurations alongside the two IL electrolytes are shown in Figure 4b,c. The corresponding LSV curves of the BASE-C and C electrodes in the Na[FSA]-[C<sub>2</sub>C<sub>1</sub>im][FSA] IL are shown in Figure 4b. Here, the anodic current of the C electrode was observed to start rising around 3.9 V at a scan rate of 1 mV s<sup>-1</sup> (threshold current density: 0.005 mA cm<sup>-2</sup>): a considerably lower anodic limit than the Pt electrode. This anodic response manifests a lower oxidation limit attributed to the influence of the conductive carbon and/or its larger surface area compared to that of the Pt electrode. This result suggests that the Na[FSA]-[C<sub>2</sub>C<sub>1</sub>im][FSA] IL is not compatible with high-voltage positive electrode materials comprising conductive carbon under practical operating conditions. In contrast, the apparent anodic current response of the BASE-C electrode in the Na[FSA]-[C<sub>2</sub>C<sub>1</sub>im][FSA] IL commenced around 3.5 V (threshold current density: 0.005 mA cm<sup>-2</sup>): indicating an even lower oxidation limit of BASE particles. Even so, this voltage range is in line with the oxidation limit of BASE previously predicted by DFT

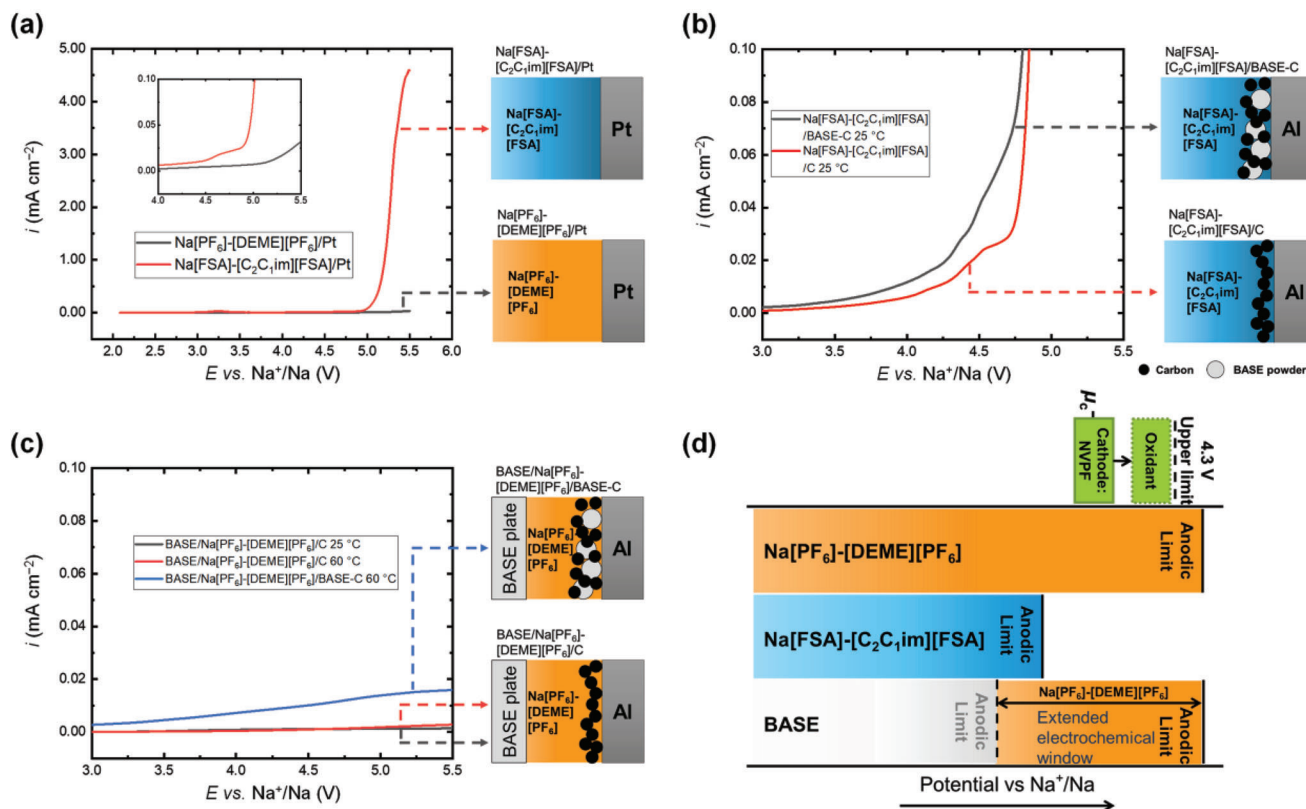


**Figure 4.** Anodic limit evaluation of the electrolytes via LSV for the Na[PF<sub>6</sub>]-[DEME][PF<sub>6</sub>], Na[FSA]-[C<sub>2</sub>C<sub>1</sub>im][FSA] ILs, BASE, and hybrid SSE. a) LSV curves of a Pt working electrode at 25 °C (Inset is the partial enlargement). Scan rate 1 mV s<sup>-1</sup>. b) LSV curves of Na[FSA]-[C<sub>2</sub>C<sub>1</sub>im][FSA] IL and BASE electrolytes with corresponding schematic illustration of BASE-C composite and C working electrodes at 25 °C. c) LSV curves of hybrid BASE/Na[PF<sub>6</sub>]-[DEME][PF<sub>6</sub>] electrolytes with corresponding schematic illustration of BASE-C composite and C working electrodes at 25 and 60 °C. Scan rate 1 mV s<sup>-1</sup>. d) Comparison of the anodic limits of Na[PF<sub>6</sub>]-[DEME][PF<sub>6</sub>], Na[FSA]-[C<sub>2</sub>C<sub>1</sub>im][FSA], BASE, and hybrid SSE by considering high-voltage electrodes such as NVPF.

calculation, as well as cyclic voltammetry results obtained at high temperatures.<sup>[12]</sup> Moreover, these LSV results indicate that both the imidazolium-based IL and BASE are not compatible with the positive electrode materials operating at voltages higher than 4 V.

For comparison, the LSV measurements were performed on hybrid BASE/Na[PF<sub>6</sub>]-[DEME][PF<sub>6</sub>] electrolytes on BASE-C electrode and C electrode at 25 and 60 °C (see Figure 4c for schematic illustration). As shown in Figure 4c, the measurements of hybrid SSE performed on C electrode at 25 °C yielded negligible current responses of 0.001 mA cm<sup>-2</sup> at 4.5 V and even below 0.002 mA cm<sup>-2</sup> at 5.2 V. It is worth noting that even when the temperature was elevated to 60 °C, the rise in current density remained moderate up to 4.7 V (threshold current density: 0.001 mA cm<sup>-2</sup>). As a comparison, the LSV curves of hybrid SSE on BASE-C electrode were observed to increase from around 3.5 V (threshold current density: 0.005 mA cm<sup>-2</sup>), in agreement with the results of Figure 4b, again indicating the oxidation behavior of the BASE powder. Na[PF<sub>6</sub>]-[DEME][PF<sub>6</sub>] IL can be expected to remain relatively stable up to 4.5 V and thus sufficiently encompass the operating voltage range of the NVPF positive electrode while acting as an interfacial layer that protects the BASE plate from decomposition. As summated in Figure 4e, the limited oxidation stability of the BASE and Na[FSA]-[C<sub>2</sub>C<sub>1</sub>im][FSA] preclude the practical deployment alongside high-voltage positive electrode

materials, whereas the introduction of a Na[PF<sub>6</sub>]-[DEME][PF<sub>6</sub>] interfacial layer extends the electrochemical window of the hybrid SSE system due to its intrinsically high oxidative stability.

### 2.3. Cell Performance

As demonstrated by the LSV analyses, introducing the Na[PF<sub>6</sub>]-[DEME][PF<sub>6</sub>] IL between the BASE and the positive electrode material suppresses the oxidation of BASE and extends the apparent oxidation limit. In efforts to harness these electrochemical benefits, a Na[PF<sub>6</sub>]-[DEME][PF<sub>6</sub>] IL interfacial layer was adopted between the BASE and the NVPF positive electrode to improve their interfacial performance. Figure 5a illustrates a Na/Na[FSA]-[C<sub>2</sub>C<sub>1</sub>im][FSA]/BASE/Na[PF<sub>6</sub>]-[DEME][PF<sub>6</sub>]/NVPF hybrid SSE cell implemented to this effect. The proposed hybrid configuration employs a Na metal negative electrode to maximize its energy density. Although Na metal is known to be electrochemically stable to BASE, the solid-solid contact also causes high interfacial resistance.<sup>[9a]</sup> Additionally, the Na/BASE interface is marked with voids that can harbor Na dendrites during Na deposition/dissolution, resulting in increased interfacial resistance, surface fractures, and, eventually, short circuits.<sup>[42]</sup> To mitigate such issues, a Na[FSA]-[C<sub>2</sub>C<sub>1</sub>im][FSA] IL was selected to serve as

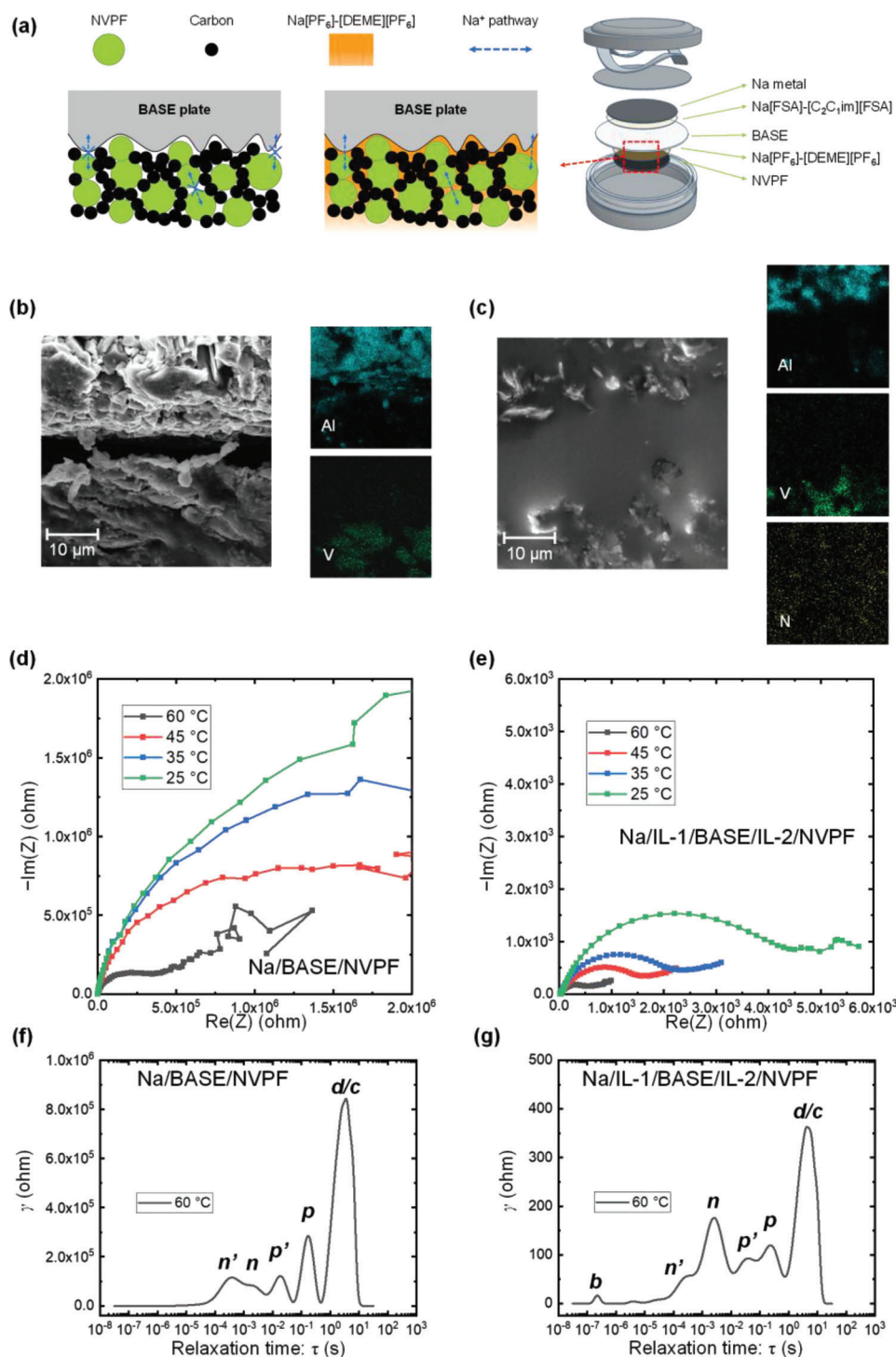


**Figure 5.** Effects of the IL layer on the interfacial properties. a) Schematic illustration of the BASE plate and positive composite electrode in the absence and presence of the IL interfacial layer and the illustration of the Na/Na[FSA]-[C<sub>2</sub>C<sub>1</sub>im][FSA]/BASE/Na[PF<sub>6</sub>]-[DEME][PF<sub>6</sub>]/NVPF prototype cell. b,c) Cross sectional SEM images of the BASE plate and positive composite electrode in the b) absence and c) presence of the IL interfacial layer with the corresponding EDX mapping results (Al, V, and N). d,e) Nyquist plots of the hybrid SSE cell: d) Na/BASE/NVPF and e) Na/Na[FSA]-[C<sub>2</sub>C<sub>1</sub>im][FSA]/BASE/Na[PF<sub>6</sub>]-[DEME][PF<sub>6</sub>]/NVPF at different temperatures. Frequency range: 0.1 Hz–10 MHz and AC amplitude: 10 mV. f,g) Results of distribution of relaxation times analysis for the corresponding impedance data of hybrid SSE cells at 60 °C.

an IL interfacial layer between the Na metal and BASE due to its high Na deposition/dissolution efficiency (see Figure S5, Supporting Information, for the cyclic voltammogram for Na metal deposition/dissolution in this IL).<sup>[43]</sup> In the Na[PF<sub>6</sub>]-[DEME][PF<sub>6</sub>] IL, Na metal deposition/dissolution is observed at 0 V versus Na<sup>+</sup>/Na, but the large polarization and low Coulombic efficiency make it less attractive for practical use for Na metal anode (Figure S6, Supporting Information). Figure 5b shows cross-sectional scanning electron microscopic (SEM) images of the interface between the BASE and NVPF positive electrode material in the absence of an IL layer. Here, the bare BASE plate marked by the coarse and rough BASE grains can be seen at the top side of the image. The bottom of the image depicts a porous surface comprising NVPF, conductive carbon, and the binder. It should also be mentioned that the present coin cell has a limited stacking pressure (provided by a single wave spring) and therefore does not allow strong direct contact between the BASE and composite electrode. As such, the numerous voids and gaps at the BASE/electrode interface, therefore, block the Na<sup>+</sup> ion paths, resulting in significantly high resistance. In comparison, introducing a Na[PF<sub>6</sub>]-[DEME][PF<sub>6</sub>] IL layer between the BASE and the electrode fills such voids and gaps and thus provides an ion transport pathway (Figure 5c). The ionic connection facilitated by the IL at the electrolyte–electrode interface was further validated by energy dispersive X-Ray (EDX) spectroscopic mapping (on the right side of the SEM image) which provided information on the individual elements of each component (Al of BASE; V of NVPF; N of Na[PF<sub>6</sub>]-[DEME][PF<sub>6</sub>]).

For insight into the effect of the IL on the interfacial contact, comparative EIS measurements were performed on the Na/BASE/NVPF and Na/Na[FSA]-[C<sub>2</sub>C<sub>1</sub>im][FSA]/BASE/Na[PF<sub>6</sub>]-[DEME][PF<sub>6</sub>]/NVPF cells at varied temperatures. As shown by the semicircles in Figure 5d,e, the introduction of the IL at the electrolyte–electrode interface significantly decreased the interfacial resistances. Moreover, increasing the operating temperatures was also noted to significantly reduce the interfacial resistance in both hybrid cell models. To distinguish the resistance components, the impedance spectra (Figure 5d,e) were further assessed through the distribution of relaxation times (DRT) analysis to identify the frequency-dependent (and thus RC time constant [ $\tau$ ] dependent) processes in the electrochemical system.<sup>[44]</sup> Figure 5f,g shows the multiple contributions in the impedance data, denoted as  $b$ ,  $n$ ,  $n'$ ,  $p$ ,  $p'$ , and  $d/c$  in their order with increasing  $\tau$  values. The differences in the vertical axis range for the proposed cells are in the order of  $10^3$ . Here, peak  $b$ , which appears in the low  $\tau$  range ( $\approx 10^{-6}$ ), is attributed to the bulk resistance.<sup>[45]</sup> The peak  $n$ , in the  $\tau$  range of  $\approx 10^{-2}$ , is assigned to the charge transfer resistance of Na<sup>+</sup> at the Na metal negative electrode. The contribution of the charge transfer reaction at the NVPF positive electrode is observed in the higher  $\tau$  range (peak  $p$ ,  $\approx 10^0$ )—in congruence with observations in previous work on a different IL electrolyte.<sup>[8]</sup> The minor peaks  $n'$  and  $p'$  observed at  $\tau$  values lower than peaks  $n$  and  $p$ , respectively, are inferred as the interfacial layers on the electrode surfaces.<sup>[45,46]</sup> The peak  $d/c$  is attributed to the ion diffusion or capacitive behavior of the cell.<sup>[45]</sup> The resistance of the electrodes and their interfaces were noted to significantly diminish with increasing temperatures (see Figure S7, Supporting Information). In Figure 5f, the large interfacial resistances

of both the negative and positive electrodes are ascribed to the absence of IL. Here, the softness of Na metal engenders a lower charge transfer resistance than that of the NVPF electrode (also see Figure S8, Supporting Information, for the Nyquist plot of NVPF/BASE/NVPF symmetric cell). On the other hand, Figure 5g exhibits remarkably diminished impedance at the electrode/BASE interface in the presence of an IL layer. This further corroborates the effectiveness of introducing IL as a strategy for improving electrolyte–electrode contact at the interface.

Batteries functioning at elevated temperatures are deemed to enhance cell chemistry efficiency and decrease the need for extensive cooling systems and thermal management, which is inherently advantageous, especially for large-scale energy storage applications.<sup>[47]</sup> Nevertheless, operation at elevated temperatures also imposes augmented thermal stability demands on the cell components including electrolytes and accelerated side reactions.<sup>[8,48]</sup> To substantiate the benefits of this IL interface more comprehensively, a hybrid SSE cell was employed for assessment at a temperature of 60 °C. As shown in Figure 6a, the electrochemical performance of the Na/Na[FSA]-[C<sub>2</sub>C<sub>1</sub>im][FSA]/BASE/Na[PF<sub>6</sub>]-[DEME][PF<sub>6</sub>]/NVPF cell was evaluated by obtaining the galvanostatic charge–discharge profiles at different current rates. The capacity is based on the weight of NVPF. Measurements performed at 60 °C were noted to yield a reversible capacity of 110 mAh g<sup>-1</sup> at 0.1C (1C = 128 mAh g<sup>-1</sup>). The cell exhibits typical electrochemical behavior of NVPF electrodes: the profiles earmarked with two-step redox plateaus at 3.7 and 4.2 V (also see the initial cycles in Figure S9, Supporting Information).<sup>[8,49]</sup> The cell provided an average voltage of 3.8 V a relatively high energy density of 416 Wh kg<sup>-1</sup> based on the weight of NVPF. The corresponding rate performance of the Na/Na[FSA]-[C<sub>2</sub>C<sub>1</sub>im][FSA]/BASE/Na[PF<sub>6</sub>]-[DEME][PF<sub>6</sub>]/NVPF cell is shown in Figure 6b, where the reversible specific capacities of 110, 108, 103, 97, and 88 mAh g<sup>-1</sup> were obtained at 0.1C, 0.2C, 0.5C, 1C, and 2C, respectively. Markedly, the high current rate of 5C attained a slightly lower capacity of 55 mAh g<sup>-1</sup> because of the occurrence of a large polarization terminated the redox plateau below the cutoff voltage of 4.3 V. Nonetheless, this cell exhibited sufficient recuperation after the rate performance test—an indication that the present hybrid SSE system is stable and reliable. The cycle performance evaluations at 1C at 60 °C (Figure 6c) manifested a highly consistent cycling performance throughout a 1500-cycle operation along with a remarkable capacity retention of 107% (compared to the first cycle) and a high average Coulombic efficiency of 99.3%. The observed increase in capacity is considered to be attributed to the progressive fracturing of NVPF particles during cycling, consequently augmenting the specific surface area of the material (Figure S10, Supporting Information). This phenomenon appears to facilitate mass transfer and increase active site which increases the capacity. Further surface characterizations were carried out on the interfaces of NVPF/BASE after 1500 cycles. X-ray photoelectron spectroscopy (XPS) disclosed the existence of a CEI on the NVPF surface (Figure S11, Supporting Information). This included prospective inorganic components such as fluoride and fluorophosphate derived from [PF<sub>6</sub>]<sup>-</sup>, as well as organic compounds comprising C–C/C–H, C–O, C=O, and C–N.<sup>[8,50]</sup> It is crucial to mention that the sole source of N-containing constituents is [DEME]<sup>+</sup>, which underscores the advantageous nature of the IL. However, no



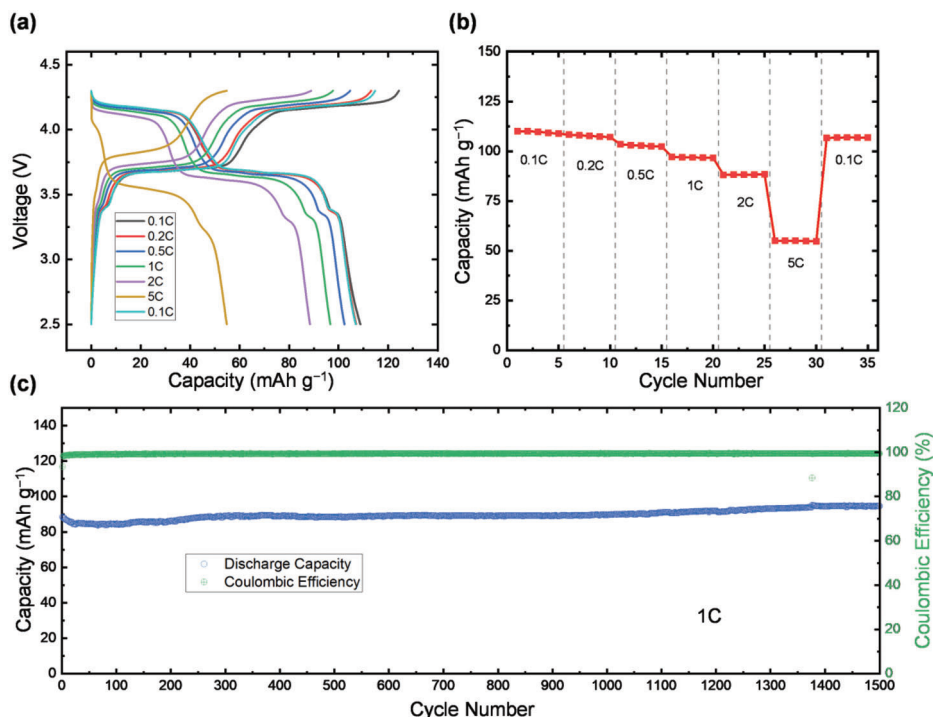


**Figure 6.** Electrochemical performance of NVPF in hybrid SSE. a) Galvanostatic charge–discharge profiles of the Na/Na[FSA]-[C<sub>2</sub>C<sub>1</sub>im][FSA]/BASE/Na[PF<sub>6</sub>]-[DEME][PF<sub>6</sub>]/NVPF cell at different rates and b) corresponding rate capability performance. c) The cyclability plot during the long-term cycling test performed at 1C.

associated component was evident on the BASE's surface, signifying that a redox reaction regarding passivation layer formation did not take place on it. Additional characterization via SEM was performed on both the pristine and cycled BASE. No substantial morphological variations were observed even after 1500 cycles as shown in Figure S12, Supporting Information. Thus, it can be concluded that beyond the high oxidative stability and electronic insulating properties of the Na[PF<sub>6</sub>]-[DEME][PF<sub>6</sub>] IL, it also mitigates oxidative decomposition of the BASE, ensuring the cell's long-term cyclability.

For a comparative evaluation, the hybrid cell configuration was subjected to analogous electrochemical measurements at 25 °C. Here, the cell demonstrated an outstanding electrochemical performance marked by a high reversible capacity of around 90 mAh g<sup>-1</sup> at 0.1C (Figures S13 and S14, Supporting Information). However, the low temperature engendered a large polarization (which is partially attributed to the relatively large thickness of the BASE plate<sup>[9a]</sup>), terminating the redox reaction of the positive electrode below the cutoff voltage of 4.3 V, resulting in diminished capacities. Nonetheless, the present study clearly demonstrates the adoption of PF<sub>6</sub>-based ILs as interfacial layers to be a judicious strategy for enhancing the anodic stability of SSEs and unlocking the capabilities of high-voltage positive electrodes in hybrid SSE batteries.

### 3. Conclusion

In conclusion, this work reports a new synthesis route entailing a fluorohydrogenate IL used to prepare the [DEME][PF<sub>6</sub>] IL (yield of 99.9% with high purity >99%). Herein, a Na[PF<sub>6</sub>]-[DEME][PF<sub>6</sub>]

IL was formulated and subjected to a series of electrochemical tests to ascertain its physical and electrochemical properties. The present IL electrolyte was found to exemplify a remarkable oxidation stability that can sufficiently accommodate high-voltage electrochemical operations. The IL was further adopted as an interfacial layer between the SSE and the positive electrode in an attempt to enhance the solid–solid contact and fill the voids prevalent at the interface. Here, the IL was found to serve a multifunctional role where it not only enhanced the oxidation limits of the BASE but also provided Na ion transport paths that help reduce the interfacial resistance engendered by the inadequate contact between the BASE and the positive electrode. The expanded electrochemical window of the hybrid SSE system was noted to improve its compatibility with high-voltage positive electrode materials, such as NVPF, thereby facilitating reliable and stable Na metal battery operations, as was demonstrated by the charge–discharge and cycle tests. The results from this study suggest that the utilization of the Na[PF<sub>6</sub>]-[DEME][PF<sub>6</sub>] IL electrolyte in the development of hybrid SSE cells is not limited to BASE and the NVPF positive electrode, but it can also be employed as a universal strategy for developing high-voltage Na metal batteries using SSEs.

### 4. Experimental Section

**Materials:** All the moisture- and air-sensitive materials were handled and prepared under a dry Ar gas atmosphere (H<sub>2</sub>O < 1 ppm and O<sub>2</sub> < 1 ppm) in a glove box (Miwa Manufacturing Co., Ltd.). The reagents used in this study: [C<sub>2</sub>C<sub>1</sub>im][FSA] (Kanto Chemical, purity > 99.9%),

Na[PF<sub>6</sub>] (FUJIFILM Wako Pure Chemical, purity: 99%), K[PF<sub>6</sub>] (FUJIFILM Wako Pure Chemical, purity: 99.5%), and Na[FSA] (Mitsubishi Materials Electronic Chemicals, purity > 99%), were all vacuum-dried at 80 °C for more than 24 h. [DEME]Br (COMBI-BLOCKS, purity > 95.0%) was dissolved in anhydrous ethanol and passed through an activated alumina column for purification, whereafter it was vacuum-dried at 80 °C. Anhydrous HF (Daikin Industries) was dried over K<sub>2</sub>NiF<sub>6</sub> prior to use. PF<sub>5</sub> gas (Kanto Denka Kogyo) was used as-supplied. BASEs plate (diameter: 16 mm; thickness: 0.75 mm) and powder (median particle diameter [D50]: 12.45 μm) were used as-purchased (BASE, Ionotec). Carbon-coated vanadium-based phosphate fluorides, Na<sub>3</sub>V<sub>2</sub>(PO<sub>4</sub>)<sub>2</sub>F<sub>3</sub> (NVPF-C) was prepared via a two-step synthesis reported by a previous study.<sup>[8]</sup>

**[DEME][PF<sub>6</sub>] Synthesis and Characterization: Ion-exchange reaction:** Stoichiometric amounts of [DEME]Br 23.55 g, 104.1 mmol) and K[PF<sub>6</sub>] (19.16 g, 104.1 mmol) were stirred in anhydrous acetone at 25 °C for 24 h in a polypropylene vessel. The resulting mixture was filtered to remove KBr and vacuum-dried at 25 °C for 24 h and subsequently at 80 °C for 24 h to remove the acetone. The crude [DEME][PF<sub>6</sub>] was repeatedly washed with deionized water until AgBr was no longer precipitated from the aqueous phase, as determined by adding 1 mol dm<sup>-3</sup> AgNO<sub>3</sub>. Upon the removal of water under vacuum at 80 °C for 72 h, 13.89 g of [DEME][PF<sub>6</sub>] (47.7 mmol) was obtained (yield 45.8%). Anal. Calc. for C<sub>8</sub>H<sub>20</sub>N<sub>1</sub>O<sub>1</sub>PF<sub>6</sub>: C, 6.9; H, 32.9; N, 4.8%. Found: C, 6.9; H 32.8; N, 4.5%. <sup>1</sup>H NMR (DMSO-*d*<sub>6</sub>), δ = 1.25 (t, 6H), 3.01 (s, 3H), 3.34 (s, 3H), 3.39 (q, 4H), 3.51 (m, 2H), 3.77 (m, 2H); <sup>19</sup>F NMR (DMSO-*d*<sub>6</sub>), δ = -72.45 (d).<sup>[29b,51]</sup>

**Lewis acid–base reaction:** The [DEME]Br (22.62 g, 100.0 mmol) and a stirring bar were placed in the PFA (tetrafluoroethylene-perfluoroalkylvinylether copolymer) reactor under the Ar atmosphere in the glove box. The entire airtight reactor was connected to a reaction line with a chemical trap filled with soda lime, as shown in Figure S2, Supporting Information. An excessive amount of HF (≈0.55 mol) was condensed on [DEME]Br at -196 °C, after which the reactor was gradually warmed up to 25 °C with the occasional release of HBr pressure. After stirring at 25 °C for 6 h, the reaction vessel was evacuated at 25 °C for 6 h to remove any unreacted HF and the HBr byproduct. The entire process (from the addition of HF to evacuation) was repeated, upon which the reactor was evacuated at 25 °C for 24 h. Subsequently, an excessive amount of PF<sub>5</sub> (more than 0.17 mol) was slowly added to the reactor. The heat from the reaction was recurrently released by cooling the reactor with liquid nitrogen. After stirring at 25 °C for 6 h, the reactor was evacuated at 25 °C for 6 h to remove any unreacted PF<sub>5</sub> and the HF product. The entire process (from the addition of PF<sub>5</sub> to evacuation) was repeated under the same conditions, and finally, the reaction vessel was evacuated at 25 °C for 24 h and again at 60 °C for 24 h. The addition of 1 mol dm<sup>-3</sup> AgNO<sub>3</sub> to the final IL did not result in the precipitation of AgBr, suggesting the absence of Br<sup>-</sup>. The water contents of the ILs were below 10 ppm according to Karl–Fischer titration (899 Coulometer, Metrohm). A pH measurement was utilized to evaluate the existence of HF in [DEME][PF<sub>6</sub>]. Approximately 0.2 g of IL was added to 10 g of water, and the pH of the water phase did not change before and after the addition of IL, indicative of the negligible amount of HF in [DEME][PF<sub>6</sub>]. Finally, 29.09 g of [DEME][PF<sub>6</sub>] (99.9 mmol) was obtained (yield 99.9%). Anal. Calc. for C<sub>8</sub>H<sub>20</sub>N<sub>1</sub>O<sub>1</sub>PF<sub>6</sub>: C, 6.9; H 32.8; N, 4.5%. Found: C, 6.8; H, 32.9, N, 4.8%. <sup>1</sup>H NMR (DMSO-*d*<sub>6</sub>), δ = 1.25 (t, 6H), 3.00 (s, 3H), 3.33 (s, 3H), 3.38 (q, 4H), 3.51 (m, 2H), 3.76 (m, 2H); <sup>19</sup>F NMR (DMSO-*d*<sub>6</sub>), δ = -70.18 (d).

**Characterization:** FT-IR spectra were recorded using an FT-IR spectrometer (ALPHA-T, Bruker Optics) in accordance with the attenuated total reflection method and with the aid of the single reflection diamond. The wavenumber range was calibrated to 4000–400 cm<sup>-1</sup>, and the resolution was set to 1 cm<sup>-1</sup>. Raman spectra were obtained using a DXR3 Smart Raman spectrometer (Thermo Fisher Scientific) equipped with a 785 nm diode-pumped solid-state laser. Elemental analyses (C, H, N) were performed using an organic elemental analyzer (Jay Science Lab JM-11). The <sup>19</sup>F and <sup>1</sup>H NMR spectra were obtained using an NMR spectrometer (JEOL ECA600) equipped with a TH5AT/FG2 probe and a 14.09637-T magnet. The <sup>1</sup>H and <sup>19</sup>F-NMR spectra were acquired at 600.1723 and 470.593 MHz, respectively. The samples were quantitatively dissolved in

dimethylsulfoxide-*d*<sub>6</sub> with quantitative amounts of trifluorotoluene standard material.

**Preparation and Characterization of Ionic Liquid Electrolytes:** ILs and sodium salts were mixed in the following molar ratios and stirred at 25 °C for 24 h: Na[PF<sub>6</sub>]-[DEME][PF<sub>6</sub>] (10:90 mol%) and Na[FSA]-[C<sub>2</sub>C<sub>1</sub>im][FSA] (20:80 mol%). An oscillating densimeter (Anton Paar, DMA4500M) was employed to measure density using ≈1 cm<sup>3</sup> of the sample measured in 5 °C increments at temperatures between 10 and 90 °C. The sample was kept at each temperature for 10 min prior to the measurement. Viscosity was measured using an electromagnetic spinning viscometer (Kyoto Electronics, EMS-1000). The sample (≈1 cm<sup>3</sup>) was loaded in a glass tube with an aluminum probe (2 mm in diameter) in the glove box and held for 10 min at temperatures between 10 and 90 °C measured at 10 °C increments. Measurements were made at a rotational rate of 600 rpm. Ionic conductivity was measured by the AC impedance method (Hioki Electric, 3532-80) with a frequency range of 100 Hz–200 kHz. The sample was loaded into an airtight T-shaped cell with two stainless steel disk electrodes in the glove box. The cell was transferred to a thermostatic chamber and held every 10 °C from 10 to 90 °C for 20 min prior to each measurement. The cell constant was determined using a standard KCl aqueous solution. The Na<sup>+</sup> transference number of Na[PF<sub>6</sub>]-[DEME][PF<sub>6</sub>] at 25 °C was calculated by measuring the bulk and diffusion resistances obtained using a symmetric Na/IL/Na via EIS at the 1 mHz–100 kHz frequency range and AC amplitude: 20 mV.

**Cell Assembly and Electrochemical Measurements:** The LSV and CV data were obtained using a 2032-type coin cell. Platinum (Niraco) and Al (Niraco) foils punched into discs (diameter: 10 mm) for use as working electrodes. The Al electrode was swept to -0.5 V versus Na<sup>+</sup>/Na to determine the Na metal deposition/dissolution property and The Pt electrode was swept to 6.5 V versus Na<sup>+</sup>/Na to determine the anodic stability. For the estimation of SSE, a BASE-C working electrode was prepared by casting BASE powder mixed with AB and PVDF in the weight ratio of 7:2:1 on Al foil, while a carbon working electrode was prepared by casting AB and PVDF in the weight ratio of 6:4 on an Al foil. A 13 mm diameter Na metal foil (Sigma-Aldrich, 99.9%) affixed onto the Al current collector was used as the counter electrode. A glass fiber separator (Whatman GF/A) was impregnated with the IL electrolyte at 60 °C under vacuum before the cell assembly. Measurements were made using an electrochemical analyzer (Bio-Logic, VSP) with a scan rate of 1 mV s<sup>-1</sup> at 25 and 60 °C.

The Na/Na[FSA]-[C<sub>2</sub>C<sub>1</sub>im][FSA]/BASE/Na[PF<sub>6</sub>]-[DEME][PF<sub>6</sub>]/NVPF hybrid solid-state cell was implemented with a sandwich-type stacking configuration using a 2032-type coin cell. The NVPF positive electrode was made by mixing the NVPF-C composite, AB, and PVDF (80:15:5) and pasting it onto Al foil (≈1 mg cm<sup>-2</sup>). The positive electrode before being dipped into the Na[PF<sub>6</sub>]-[DEME][PF<sub>6</sub>] (10:90 mol%) IL under vacuum and then transferred to the coin cell. The corresponding electrolyte/capacity ratio was 6.8 μL mAh<sup>-1</sup>. Sodium metal (Sigma-Aldrich Chemistry, purity: 99.95%) was cut into a disk (12 mm diameter) and affixed onto an Al plate current collector as the negative electrode. One drop of Na[FSA]-[C<sub>2</sub>C<sub>1</sub>im][FSA] (20:80 mol%) was added between Na and BASE to improve the contact of the interface and facilitate Na deposition/dissolution.

EIS measurements were carried out in the 15–60 °C temperature range, 0.1–10<sup>6</sup> Hz frequency range, and an AC amplitude of 10 mV. The DRT analysis was performed using the DRTtools package on the MATLAB software.<sup>[44]</sup> All electrochemical tests were carried out after 6 h rest to attain the temperature equilibrium. For the charge–discharge test, a current density based on the theoretical capacity of NVPF (1C = 128 mA g<sup>-1</sup>) was adopted. The lower and upper cutoff voltages were set at 2.5 and 4.3 V, respectively. Charge–discharge characteristics, rate capabilities, and cycling performances were assessed using a HJ1001SD8 test device (Hokuto Denko). The CEI layer components were analyzed using XPS (JEOL, JPS-9030, Mg Kα source).

## Supporting Information

Supporting Information is available from the Wiley Online Library or from the author.

## Acknowledgements

This study was supported by JSPS Grant-in-Aid for Scientific Research (B) Grant Number 21H02047. D.W. thanks the China Scholarship Council (CSC) for the financial support.

## Conflict of Interest

The authors declare no conflict of interest.

## Author Contributions

D.W.: Investigation, Data Curation, Visualization, Writing-Original draft. M.T.: Investigation. J.H.: Conceptualization, Methodology, Investigation, Writing-Original draft, Review and Editing. K.M.: Investigation, Validation, Supervision, Funding acquisition, Writing-Review and Editing, Revision and Suggestions. R.H.: Supervision, Writing-Review and Editing, Revision and Suggestions.

## Data Availability Statement

The data that support the findings of this study are available from the corresponding author upon reasonable request.

## Keywords

anodic limits, high voltage electrodes, hybrid solid-state electrolytes, ionic liquids, sodium secondary batteries

Received: April 5, 2023  
Revised: June 2, 2023  
Published online: June 22, 2023

- [1] Y. You, A. Manthiram, *Adv. Energy Mater.* **2018**, *8*, 1701785.
- [2] a) D. H. Lee, J. Xu, Y. S. Meng, *Phys. Chem. Chem. Phys.* **2013**, *15*, 3304; b) P.-F. Wang, Y. You, Y.-X. Yin, Y.-G. Guo, *J. Mater. Chem. A* **2016**, *4*, 17660; c) A. Konarov, H. J. Kim, J.-H. Jo, N. Voronina, Y. Lee, Z. Bakenov, J. Kim, S.-T. Myung, *Adv. Energy Mater.* **2020**, *10*, 2001111.
- [3] Y.-U. Park, D.-H. Seo, H. Kim, J. Kim, S. Lee, B. Kim, K. Kang, *Adv. Funct. Mater.* **2014**, *24*, 4603.
- [4] a) A. Ponrouch, E. Marchante, M. Courty, J.-M. Tarascon, M. R. Palacin, *Energy Environ. Sci.* **2012**, *5*, 8572; b) H. Che, S. Chen, Y. Xie, H. Wang, K. Amine, X.-Z. Liao, Z.-F. Ma, *Energy Environ. Sci.* **2017**, *10*, 1075; c) H.-J. Liang, Z.-Y. Gu, X.-X. Zhao, J.-Z. Guo, J.-L. Yang, W.-H. Li, B. Li, Z.-M. Liu, W.-L. Li, X.-L. Wu, *Angew. Chem., Int. Ed.* **2021**, *60*, 26837; d) J. U. Choi, J. H. Jo, Y. J. Park, K.-S. Lee, S.-T. Myung, *Adv. Energy Mater.* **2020**, *10*, 2001346.
- [5] a) K. Subramanyan, Y.-S. Lee, V. Aravindan, *J. Colloid Interface Sci.* **2021**, *582*, 51; b) J.-J. Fan, P. Dai, C.-G. Shi, Y. Wen, C.-X. Luo, J. Yang, C. Song, L. Huang, S.-G. Sun, *Adv. Funct. Mater.* **2021**, *31*, 2010500.
- [6] A. Ponrouch, R. Dedryvère, D. Monti, A. E. Demet, J. M. A. Mba, L. Croguennec, C. Masquelier, P. Johansson, M. R. Palacin, *Energy Environ. Sci.* **2013**, *6*, 2361.
- [7] J. Chen, Y. Peng, Y. Yin, M. Liu, Z. Fang, Y. Xie, B. Chen, Y. Cao, L. Xing, J. Huang, Y. Wang, X. Dong, Y. Xia, *Energy Environ. Sci.* **2022**, *15*, 3360.
- [8] J. Hwang, K. Matsumoto, R. Hagiwara, *Adv. Energy Mater.* **2020**, *10*, 2001880.
- [9] a) M. P. Fertig, K. Skadell, M. Schulz, C. Dirksen, P. Adelhelm, M. Stelter, *Batteries Supercaps* **2022**, *5*, 202100131; b) P. Minnmann, F. Strauss, A. Bielefeld, R. Ruess, P. Adelhelm, S. Burkhardt, S. L. Dreyer, E. Trevisanello, H. Ehrenberg, T. Brezesinski, F. H. Richter, J. Janek, *Adv. Energy Mater.* **2022**, *12*, 2201425.
- [10] D. Wang, J. Hwang, C. Y. Chen, K. Kubota, K. Matsumoto, R. Hagiwara, *Adv. Funct. Mater.* **2021**, *31*, 2105524.
- [11] a) H. Yamauchi, J. Ikejiri, F. Sato, H. Oshita, T. Honma, T. Komatsu, *J. Am. Ceram. Soc.* **2019**, *102*, 6658; b) H. Yamauchi, J. Ikejiri, K. Tsunoda, A. Tanaka, F. Sato, T. Honma, T. Komatsu, *Sci. Rep.* **2020**, *10*, 9453.
- [12] a) J. Zeising, C. Vanvoren, J. L. Souquet, *Electrochim. Acta* **1981**, *26*, 145; b) R. Ansell, *J. Mater. Sci.* **1986**, *21*, 365; c) V. Lacivita, Y. Wang, S.-H. Bo, G. Ceder, *J. Mater. Chem. A* **2019**, *7*, 8144.
- [13] a) A. M. Nolan, Y. Liu, Y. Mo, *ACS Energy Lett.* **2019**, *4*, 2444; b) B. Tang, P. W. Jaschin, X. Li, S.-H. Bo, Z. Zhou, *Mater. Today* **2020**, *41*, 200.
- [14] a) Y. Tian, T. Shi, W. D. Richards, J. Li, J. C. Kim, S.-H. Bo, G. Ceder, *Energy Environ. Sci.* **2017**, *10*, 1150; b) Y. Lu, L. Li, Q. Zhang, Z. Niu, J. Chen, *Joule* **2018**, *2*, 1747.
- [15] C.-Z. Zhao, B.-C. Zhao, C. Yan, X.-Q. Zhang, J.-Q. Huang, Y. Mo, X. Xu, H. Li, Q. Zhang, *Energy Storage Mater.* **2020**, *24*, 75.
- [16] a) J.-K. Kim, Y. J. Lim, H. Kim, G.-B. Cho, Y. Kim, *Energy Environ. Sci.* **2015**, *8*, 3589; b) W. Hou, X. Guo, X. Shen, K. Amine, H. Yu, J. Lu, *Nano Energy* **2018**, *52*, 279; c) D. Lei, Y.-B. He, H. Huang, Y. Yuan, G. Zhong, Q. Zhao, X. Hao, D. Zhang, C. Lai, S. Zhang, J. Ma, Y. Wei, Q. Yu, W. Lv, Y. Yu, B. Li, Q.-H. Yang, Y. Yang, J. Lu, F. Kang, *Nat. Commun.* **2019**, *10*, 4244; d) H. K. Tran, B. T. Truong, B.-R. Zhang, R. Jose, J.-K. Chang, C.-C. Yang, *ACS Appl. Energy Mater.* **2023**, *6*, 1475.
- [17] a) L. Liu, X. Qi, Q. Ma, X. Rong, Y.-S. Hu, Z. Zhou, H. Li, X. Huang, L. Chen, *ACS Appl. Mater. Interfaces* **2016**, *8*, 32631; b) Z. Zhang, Q. Zhang, J. Shi, Y. S. Chu, X. Yu, K. Xu, M. Ge, H. Yan, W. Li, L. Gu, Y.-S. Hu, H. Li, X.-Q. Yang, L. Chen, X. Huang, *Adv. Energy Mater.* **2017**, *7*, 1601196; c) J. Hwang, K. Matsumoto, C.-Y. Chen, R. Hagiwara, *Energy Environ. Sci.* **2021**, *14*, 5834.
- [18] a) Y. Zheng, S. Tawa, J. Hwang, Y. Orikasa, K. Matsumoto, R. Hagiwara, *Chem. Mater.* **2021**, *33*, 868; b) S. Kaushik, K. Matsumoto, Y. Orikasa, M. Katayama, Y. Inada, Y. Sato, K. Gotoh, H. Ando, R. Hagiwara, *J. Power Sources* **2021**, *483*, 229182; c) S. Zhang, J. Hwang, K. Matsumoto, R. Hagiwara, *ACS Appl. Mater. Interfaces* **2022**, *14*, 19426; d) Y. Zheng, D. Wang, S. Kaushik, S. Zhang, T. Wada, J. Hwang, K. Matsumoto, R. Hagiwara, *EnergyChem* **2022**, *4*, 100075.
- [19] M. Ue, M. Takeda, M. Takehara, S. Mori, *J. Electrochem. Soc.* **1997**, *144*, 2684.
- [20] a) M. Ue, A. Murakami, S. Nakamura, *J. Electrochem. Soc.* **2002**, *149*, A1572; b) S. P. Ong, O. Andreussi, Y. Wu, N. Marzari, G. Ceder, *Chem. Mater.* **2011**, *23*, 2979.
- [21] P. Peljo, H. H. Girault, *Energy Environ. Sci.* **2018**, *11*, 2306.
- [22] J. Golding, N. Hamid, D. R. MacFarlane, M. Forsyth, C. Forsyth, C. Collins, J. Huang, *Chem. Mater.* **2001**, *13*, 558.
- [23] K. R. Harris, L. A. Woolf, M. Kanakubo, *J. Chem. Eng. Data* **2005**, *50*, 1777.
- [24] Y. Yoshimura, T. Takekiyo, Y. Imai, H. Abe, *J. Phys. Chem. C* **2012**, *116*, 2097.
- [25] T. Sato, G. Masuda, K. Takagi, *Electrochim. Acta* **2004**, *49*, 3603.
- [26] H. Matsumoto, H. Sakaebe, K. Tatsumi, *ECS Trans.* **2009**, *16*, 59.
- [27] a) R. K. B. Gover, A. Bryan, P. Burns, J. Barker, *Solid State Ionics* **2006**, *177*, 1495; b) M. Bianchini, N. Brisset, F. Fauth, F. Weill, E. Elkaim, E. Suard, C. Masquelier, L. Croguennec, *Chem. Mater.* **2014**, *26*, 4238; c) C. Zhu, C. Wu, C.-C. Chen, P. Kopold, P. A. van Aken, J. Maier, Y. Yu, *Chem. Mater.* **2017**, *29*, 5207.
- [28] S. K. Singh, A. W. Savoy, *J. Mol. Liq.* **2020**, *297*, 112038.
- [29] a) K. Matsumoto, R. Hagiwara, Y. Ito, *J. Fluorine Chem.* **2002**, *115*, 133; b) K. Matsumoto, R. Hagiwara, R. Yoshida, Y. Ito, Z. Mazej, P. Benkič, B. Žemva, O. Tamada, H. Yoshino, S. Matsubara, *Dalton Trans.* **2004**, *144*

- [30] a) R. Hagiwara, T. Hirashige, T. Tsuda, Y. Ito, *J. Fluorine Chem.* **1999**, 99, 1; b) R. Hagiwara, T. Hirashige, T. Tsuda, Y. Ito, *J. Electrochem. Soc.* **2002**, 149, D1; c) R. Hagiwara, K. Matsumoto, Y. Nakamori, T. Tsuda, Y. Ito, H. Matsumoto, K. Momota, *J. Electrochem. Soc.* **2003**, 150, D195.
- [31] A. M. Heyns, C. W. F. T. Pistorius, *Spectrochim. Acta, Part A* **1974**, 30, 99.
- [32] T. Moumene, E. H. Belarbi, B. Haddad, D. Villemin, O. Abbas, B. Khelifa, S. Bresson, *J. Mol. Struct.* **2015**, 1083, 179.
- [33] a) S. Tsuge, K. Uno, T. Hanasaki, T. Takekiyo, H. Abe, Y. Yoshimura, *J. Mol. Struct.* **2014**, 1060, 208; b) H. Abe, F. Nemoto, H. Kishimura, S. Ozawa, *J. Mol. Liq.* **2020**, 315, 113687.
- [34] K. Matsumoto, T. Hosokawa, T. Nohira, R. Hagiwara, A. Fukunaga, K. Numata, E. Itani, S. Sakai, K. Nitta, S. Inazawa, *J. Power Sources* **2014**, 265, 36.
- [35] a) F. Wohde, M. Balabajew, B. Roling, *J. Electrochem. Soc.* **2016**, 163, A714; b) B. Scrosati, F. Croce, L. Persi, *J. Electrochem. Soc.* **2000**, 147, 1718.
- [36] a) H. Vogel, *Phys. Z.* **1921**, 22, 645; b) G. S. Fulcher, *J. Am. Ceram. Soc.* **1925**, 8, 339; c) W. Xu, E. I. Cooper, C. A. Angell, *J. Phys. Chem. B* **2003**, 107, 6170.
- [37] P. Walden, *Z. Phys. Chem.* **1906**, 55U, 207.
- [38] K. R. Harris, *J. Phys. Chem. B* **2019**, 123, 7014.
- [39] a) C. Schreiner, S. Zugmann, R. Hartl, H. J. Gores, *J. Chem. Eng. Data* **2010**, 55, 1784; b) K. R. Harris, *J. Phys. Chem. B* **2010**, 114, 9572.
- [40] F. Han, T. Gao, Y. Zhu, K. J. Gaskell, C. Wang, *Adv. Mater.* **2015**, 27, 3473.
- [41] a) F. Han, Y. Zhu, X. He, Y. Mo, C. Wang, *Adv. Energy Mater.* **2016**, 6, 1501590; b) T. K. Schwietert, V. A. Arszewska, C. Wang, C. Yu, A. Vasileiadis, N. J. J. de Klerk, J. Hageman, T. Hupfer, I. Kerkamm, Y. Xu, E. van der Maas, E. M. Kelder, S. Ganapathy, M. Wagemaker, *Nat. Mater.* **2020**, 19, 428.
- [42] a) R. Haas, C. Pompe, M. Osenberg, A. Hilger, I. Manke, B. Mogwitz, U. Maitra, D. Langsdorf, D. Schröder, *Energy Technol.* **2019**, 7, 1801146; b) G. J. Rees, D. S. Jolly, Z. Ning, T. J. Marrow, G. E. Pavlovskaya, P. G. Bruce, *Angew. Chem., Int. Ed.* **2021**, 60, 2110; c) D. S. Jolly, Z. Ning, J. E. Darnbrough, J. Kasemchainan, G. O. Hartley, P. Adamson, D. E. J. Armstrong, J. Marrow, P. G. Bruce, *ACS Appl. Mater. Interfaces* **2020**, 12, 678.
- [43] a) T. Hosokawa, K. Matsumoto, T. Nohira, R. Hagiwara, A. Fukunaga, S. Sakai, K. Nitta, *J. Phys. Chem. C* **2016**, 120, 9628; b) M. Forsyth, H. Yoon, F. Chen, H. Zhu, D. R. MacFarlane, M. Armand, P. C. Howlett, *J. Phys. Chem. C* **2016**, 120, 4276.
- [44] T. H. Wan, M. Saccoccio, C. Chen, F. Ciucci, *Electrochim. Acta* **2015**, 184, 483.
- [45] M. Hahn, D. Rosenbach, A. Krimalowski, T. Nazarenus, R. Moos, M. Thelakkat, M. A. Danzer, *Electrochim. Acta* **2020**, 344, 136060.
- [46] J. Illig, M. Ender, T. Chrobak, J. P. Schmidt, D. Klotz, E. Ivers-Tiffée, *J. Electrochem. Soc.* **2012**, 159, A952.
- [47] a) M.-T. F. Rodrigues, G. Babu, H. Gullapalli, K. Kalaga, F. N. Sayed, K. Kato, J. Joyner, P. M. Ajayan, *Nat. Energy* **2017**, 2, 17108; b) X. Lin, M. Salari, L. M. R. Arava, P. M. Ajayan, M. W. Grinstaff, *Chem. Soc. Rev.* **2016**, 45, 5848; c) J. Wang, W. Huang, A. Pei, Y. Li, F. Shi, X. Yu, Y. Cui, *Nat. Energy* **2019**, 4, 664.
- [48] a) Y. Feng, L. Zhou, H. Ma, Z. Wu, Q. Zhao, H. Li, K. Zhang, J. Chen, *Energy Environ. Sci.* **2022**, 15, 1711; b) C. Wang, D. Du, M. Song, Y. Wang, F. Li, *Adv. Energy Mater.* **2019**, 9, 1900022; c) Z. Li, Y. Zhang, J. Zhang, Y. Cao, J. Chen, H. Liu, Y. Wang, *Angew. Chem., Int. Ed.* **2022**, 61, e202116930.
- [49] X. Zhang, X. Rui, D. Chen, H. Tan, D. Yang, S. Huang, Y. Yu, *Nanoscale* **2019**, 11, 2556.
- [50] S. Wang, C. Li, X. Fan, S. Wen, H. Lu, H. Dong, J. Wang, Y. Quan, S. Li, *Energy Technol.* **2021**, 9, 2100190.
- [51] K. Yuyama, G. Masuda, H. Yoshida, T. Sato, *J. Power Sources* **2006**, 162, 1401.